

# Theoretical Modeling of Tunneling Barriers in Carbon-Based Molecular Electronic Junctions

Mykola Kondratenko,<sup>†,‡</sup> Stanislav R. Stoyanov,<sup>†,§,||</sup> Sergey Gusarov,<sup>†</sup> Andriy Kovalenko,<sup>†,||</sup> and Richard L. McCreery<sup>\*,†,‡</sup>

<sup>†</sup>National Institute for Nanotechnology, National Research Council, Edmonton, Alberta T6G 2M9, Canada

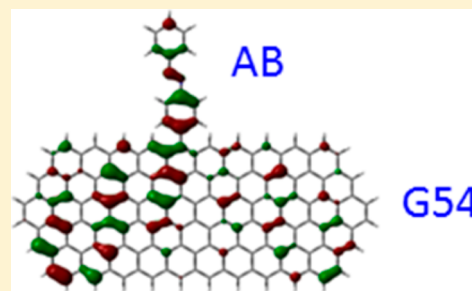
<sup>‡</sup>Department of Chemistry, University of Alberta, Edmonton, Alberta T6G 2R3, Canada

<sup>§</sup>Department of Chemical and Materials Engineering, University of Alberta, Edmonton, Alberta T6G 2V4, Canada

<sup>||</sup>Department of Mechanical Engineering, University of Alberta, Edmonton, Alberta T6G 2G8, Canada

## S Supporting Information

**ABSTRACT:** Density functional theory (DFT) is applied to three models for carbon-based molecular junctions containing fragments of graphene with covalent edge-bonding to aromatic and aliphatic molecules, with the graphene representing a  $sp^2$  hybridized carbon electrode and the molecule representing a molecular layer between two electrodes. The DFT results agree well with experimental work functions and transport barriers, including the electronic coupling between molecular layers and graphitic contacts, and predict the compression of tunnel barriers observed for both ultraviolet photoelectron spectroscopy (UPS) and experimental tunneling currents. The results reveal the strong effect of the dihedral angle between the planes of the graphene electrode and the aromatic molecule and imply that the molecules with the smallest dihedral angle are responsible for the largest local current densities. In addition, the results are consistent with the proposal that the orbitals which mediate tunneling are those with significant electron density in the molecular layer. These conclusions should prove valuable for understanding the relationships between molecular structure and electronic transport as an important step toward rational design of carbon-based molecular electronic devices.



## INTRODUCTION

Molecular electronics involves the development of electronic devices containing molecules oriented between electrodes by either covalent bonding or physisorption. A major goal of the field of molecular electronics is to integrate molecules as components in microelectronic circuits and control electronic transport by manipulating the device architecture. There are two main device constructs containing a single molecule and an ensemble of molecules, either covalently bonded or adsorbed to the electrode. The relationship between molecular structure and electron transport is essential to device design and practical applications. It is important to understand how molecular energy levels affect charge transport through single molecules or arrays of oriented molecules. Of particular interest to our study are devices containing nanoscale molecular layers with thickness in the range of 1–20 nm. Numerous experimental observations of charge transport through molecular junctions have been reported and several theoretical treatments have been proposed to explain the experimental results. The latter are often categorized as the “Simmons” approach based on tunnelling through a thin film<sup>1–7</sup> and the “Landauer” approach that considers the probability of electron tunnelling through a single molecule.<sup>8–14</sup> There has been significant progress in correlating theory with experimental results for transport in molecular junctions,<sup>10,15–23</sup> although the problem is compli-

cated by concerns about structural disorder, limitations of various modeling approaches, electronic interactions between the molecules and the contacts, and experimental uncertainty.<sup>24–27</sup>

Our laboratory has developed “ensemble” molecular junctions made by bonding aromatic molecules covalently to  $sp^2$  hybridized carbon substrates, followed by vapor deposition of metal or carbon top contacts.<sup>28–32</sup> The carbon substrate material is pyrolyzed photoresist film (PPF), a metallic conductor ( $\rho = 0.006 \Omega\text{-cm}$ ) with near-atomic flatness ( $<0.4$  nm rms by AFM), which forms covalent bonds with aromatic radicals produced by reduction of diazonium reagents.<sup>33,34</sup> Although the bonded molecules do not “assemble” into the ordered arrangement of more common Au/thiol self-assembled monolayers, they tolerate vapor deposition of Cu or carbon top contacts to produce junctions containing 2–22 nm thick molecular layers with high yield ( $>80\%$  nonshorted devices). Finished devices remain unaltered over a wide temperature range (5 to 625 K),<sup>2,35</sup> or current/voltage cycling for  $>10^9$  cycles<sup>2</sup> to  $\pm 0.6$  A/cm<sup>2</sup>. These devices are fabricated in parallel using conventional photolithographic processing<sup>36</sup> and are

Received: September 29, 2014

Revised: April 25, 2015

Published: April 30, 2015

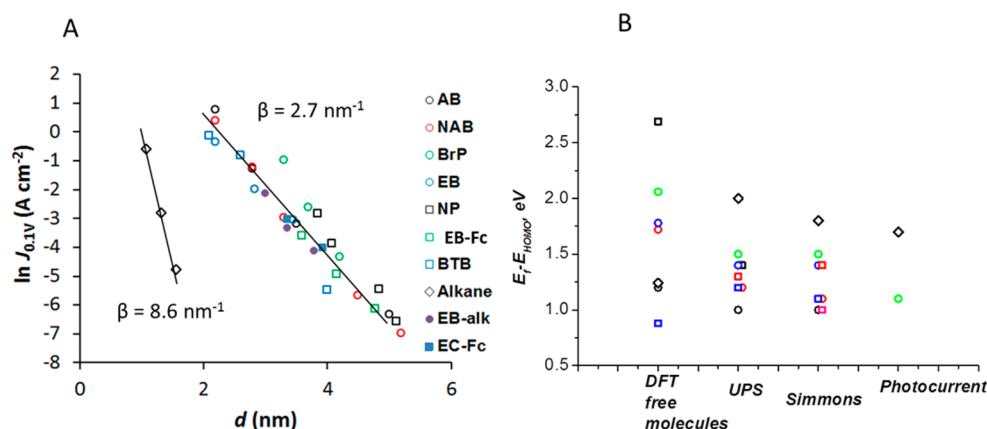


**Figure 1.** (A) Attenuation plots for PPF/molecule/Cu molecular junctions containing multilayers of the indicated molecules, with thicknesses verified by atomic force microscopy (AFM).<sup>33</sup> AB = azobenzene, NAB = nitroazobenzene, BrP = bromophenyl, EB = ethynyl benzene, NP = nitrophenyl, AQ = anthraquinone, BTB = bithienylbenzene, alkane = aminoalkane series, EB-Alk = ethynyl benzene-triazole-alkane, EB-Fc = ethynyl benzene-triazole-ferrocene. (B) Tunneling barriers calculated as  $E_f - E_{\text{HOMO}}$  from free molecule HOMO energies [BLYP-6-31G(d)] with  $E_f$  predicted from the PPF Fermi level (DFT free molecules) and experimentally determined from UPS,  $JV$  results fitted to the Simmons equation, and photocurrent measurements. Results compiled from refs 30, 37, 39. All results are experimental except the first column of panel B.

tolerant to etching reagents, photoresist, and developers after completion.<sup>35</sup> For PPF/molecule/Cu junctions in the thickness range of 2.2–5.2 nm, the transport mechanism is consistent with tunneling and the small observed temperature dependence is due to broadening of the contact Fermi function.<sup>2</sup>

A detailed investigation of >400 junctions containing a series of eight aromatic molecules and an alkane was undertaken to explore the effect of molecular orbital energy levels on tunneling current. The study was also intended to test the common assumption that the barrier for electron tunneling is  $E_{\text{LUMO}} - E_f$  where  $E_f$  is the contact Fermi level and  $E_{\text{LUMO}}$  is the energy of the lowest unoccupied molecular orbital, whereas the hole tunneling barrier is  $E_f - E_{\text{HOMO}}$ , where  $E_{\text{HOMO}}$  is the energy of the highest occupied molecular orbital. As noted in past reports,<sup>2,30</sup> transport in PPF/molecule/Cu junctions studied to date is consistent with hole tunneling, and the free molecule HOMO levels are closer than the LUMOs to the contact Fermi level of  $-4.8$  eV (relative to vacuum). In the series of eight aromatic molecules studied, the  $E_{\text{HOMO}}$  of the free molecules varied by more than 2 eV; however, in the PPF/molecule/Cu junctions, the tunneling currents were very similar with an average attenuation constant ( $\beta$ ) of  $2.7 \pm 0.6 \text{ nm}^{-1}$ .<sup>30</sup> Fabrication of additional junctions using “click” chemistry produced similar results,<sup>37</sup> as summarized in Figure 1A. The attenuation coefficients and current densities of the junctions containing aromatic molecules were similar to each other but differed statistically from those containing an alkane molecule ( $\beta = 8.6 \text{ nm}^{-1}$ ). Analysis of current density/voltage ( $JV$ ) curves using the Simmons model with image charge and effective mass corrections yielded barrier heights of  $1.25 \pm 0.2$  eV for the aromatic molecules and 1.8 eV for the alkane.<sup>30</sup> Ultraviolet photoelectron spectroscopy (UPS) of PPF/molecule surfaces yielded  $E_f - E_{\text{HOMO}}$  of  $1.32 \pm 0.2$  eV for the aromatic molecules and 1.8 eV for the alkane.<sup>2,30,38</sup> In addition, energy levels of the intact PPF/molecule/Cu junctions were determined independently using photocurrent measurements, yielding  $E_f - E_{\text{HOMO}}$  values of  $1.0 \pm 0.1$  eV for a bromophenyl junction and  $1.7 \pm 0.1$  eV for an alkane ( $\text{NHC}_{12}\text{H}_{25}$ ).<sup>39</sup> These results are summarized in Figure 1B, plotted as  $E_f - E_{\text{HOMO}}$  calculated for the free molecules and determined from experimental transport, UPS, and photo-

current measurements. The  $E_f - E_{\text{HOMO}}$  predicted from the free molecule and PPF energy levels yield tunneling barriers in the range 0.7 to 2.0 eV for the aromatic molecules, which would correspond to a  $>10^6 \text{ A/cm}^2$  range of current densities based on the Simmons analysis. However, the UPS, transport, and photocurrent measurements consistently indicate a substantially smaller variation in  $E_f - E_{\text{HOMO}}$ , which we termed “compression” of the predicted tunneling barriers to a near-constant value of  $\sim 1.3$  eV for the aromatic molecules.<sup>30</sup> This compression was attributed to a violation of the Mott–Schottky rule due to strong electronic coupling between the aromatic  $\pi$  system of the PPF and the aromatic molecules, with partial charge transfer between the molecular layer and the contacts. Similar effects on energy barriers have been described in detail for semiconductor/molecule and metal/molecule interfaces, and are often discussed in the context of “vacuum level alignment”.<sup>4,40–44</sup> The results for PPF/molecule/Cu junctions strongly indicate that the contacts and molecules must be considered as one electronic system which only partially reflects the properties of the isolated components.<sup>30</sup>

The electronic interactions between contacts and molecules manifested in Figure 1 complicate attempts to model molecular junctions computationally, because the real system is much larger than a single molecule. The current report addresses two general questions ultimately directed toward rational design of carbon-based molecular junctions.

First, can available density functional and related theoretical tools be used to model molecules bonded to PPF with sufficient accuracy to have predictive value? Although the interface between an aromatic molecule and PPF is not structurally completely defined, it is unique in possessing a covalent, conjugated bond between the contact surface and the molecular layer. A theoretical procedure validated by experimental observations should provide useful insights into the consequences of this unique arrangement. Second, can theory account for the compression of the tunneling barriers apparent in Figure 1B, and provide insight into the effects of vacuum level alignment? If so, theory may provide guidance on how to avoid or increase the compression effect, information that should be relevant to any attempts to rationally design molecular junctions. We employ models of PPF based on a

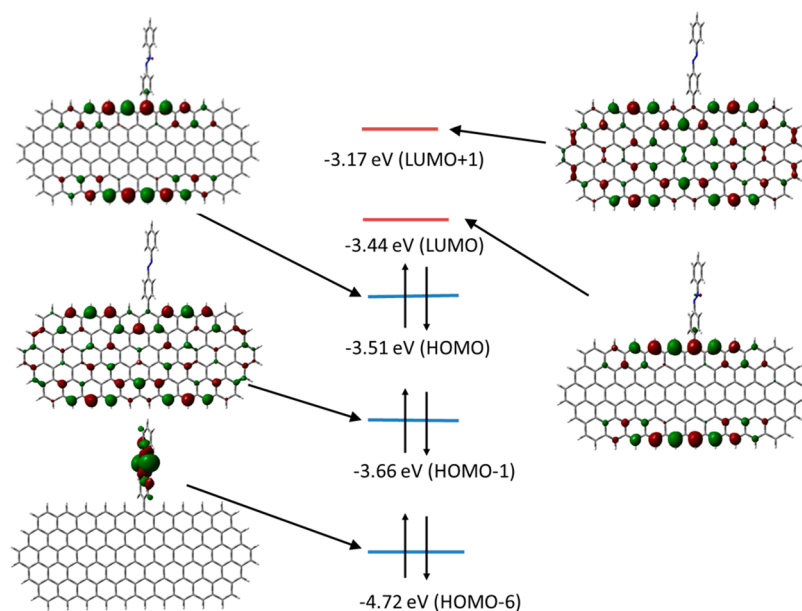


**Figure 2.** Spatial distribution and energy diagram of five orbitals of a G54-AB structure calculated using Model 1. Energies are relative to vacuum. H-6 is the occupied orbital closest in energy to the PPF Fermi level having significant electron density on the AB molecule.

graphene sheet, with and without molecules covalently bonded to the graphene edge. This approach permits assessment of the size of graphene sheet and the level of theory required to accurately predict experimental observables such as work function and  $E_f - E_{\text{HOMO}}$ . Following validation with UPS, transport, and photocurrent measurements already reported, the theory will then provide useful insights into the orbitals that mediate tunneling and the factors that govern the electronic response of PPF/molecule/Cu molecular junctions.

## COMPUTATIONAL TECHNIQUE

Chemisorbed molecules considered are azobenzene (AB), nitroazobenzene (NAB), nitrophenyl (NP), bromobenzene (PhBr), ethynylbenzene (EB), 5-phenyl-2,2'-bithiophene (BTB), anthraquinone (AQ), and amino-octane (C8), all bonded to the edge of an  $sp^2$  carbon fragment. Although many of the experimental devices are multilayers of 2–5 molecular units, only the monomers are considered here. Calculations are based on three models (see Supporting Information, Figure S1), each containing two parts: a graphene nanoribbon of different dimensions representing the electrode and a single molecule covalently bonded to the electrode surface representing the molecular layer. The models are defined as follows.

**Model 1.** The electrode is a planar 54-ring graphene fragment (G54) and the molecules are bonded to its long zigzag edge. In order to maintain consistency across the three models, the geometry optimization in Model 1 is performed using the BLYP density functional with a 6-31G(d) basis set as implemented in Gaussian 09 computational chemistry software suite.<sup>45</sup> Also, single point calculations for the structure with preset dihedral angle between planes representing molecular and electrode parts are performed using the same BLYP/6-31G(d) method, by setting the dihedral angle to a desired value following previous geometry optimization.

**Model 2.** The electrode is a periodically extended graphene nanoribbon with molecules bonded to the zigzag edge. The system is modeled using periodic boundary conditions (PBC) as a triclinic periodic cell with  $a$ ,  $b$  and  $c$  cell lengths of 6.000,

0.984, and 0.680 nm, respectively (axes are shown in Supporting Information, Figure 1). The distance between graphene planes in this model (corresponding to cell length  $c$ ) is greater than twice that of graphite (0.335 nm) to prevent interplanar interactions, thus representing an array of infinitely long but noninteracting ribbons. Geometry optimization of all the Model 2 structures is performed by using the gradient-corrected BLYP<sup>46</sup> density functional and double numerical basis set with polarization function for H atom (DNP),<sup>47</sup> as implemented in the DMol<sup>3</sup> computational chemistry software.<sup>48</sup> An extra fine numerical integration grid that contains 474 angular points is used. Brillouin zone sampling is restricted to the  $\Gamma$  point. Also, single point calculations for the structure with preset dihedral angle between planes representing molecular and electrode parts are performed by setting the dihedral angle to a desired value following previous geometry optimization using the BLYP/DNP method.

**Model 3.** The electrode is a periodically extended graphite slice cut perpendicular to the sheet plane and takes into account the interplanar interactions of infinitely long graphene ribbons with molecules bonded to the zigzag edge. The system is modeled using PBC as a triclinic periodic cell with  $a$ ,  $b$ , and  $c$  cell lengths of 6.000, 0.984, and 0.680 nm, respectively. In this model, two graphene layers with offset 0.142 nm and distance 0.335 nm between planes are introduced in the unit cell and the edge of only one plane is modified with molecules. The calculations for Model 3 are performed by using the same density functionals, basis set, integration grid, and Brillouin zone sampling as described for Model 2. The single point calculations are performed to study the effect of molecule-electrode dihedral angle, as in Model 2.

Orbital diagrams in Figures 2, 3, 5, and 6 are plotted with an isovalue = 0.02  $e/\text{au}^3$  for all three models. This isovalue is typical of those used for clearly indicating electron localization and is the default for Gaussview software.<sup>45</sup> The orbital isosurfaces depicted in the figures represent the localization of the electron density of a particular orbital.

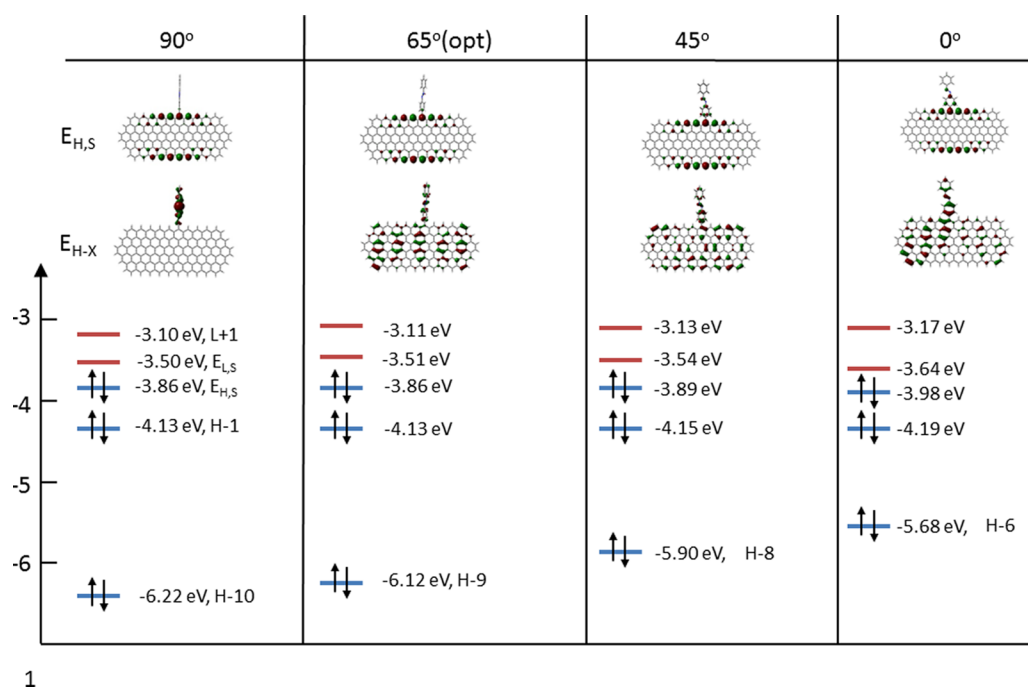


**Figure 3.** Variation in orbital energies of G54–AB structure as a function of the dihedral angle between the planes of the G54 sheet and the AB aromatic rings. Dihedral angle of 65° corresponds to the fully optimized structure with minimum energy,  $E_{H,S}$  is the HOMO of the G54–AB cluster, and  $E_{H-X}$  is the energy of the highest energy occupied molecular orbital with significant electron localization on the AB moiety.

## RESULTS AND DISCUSSION

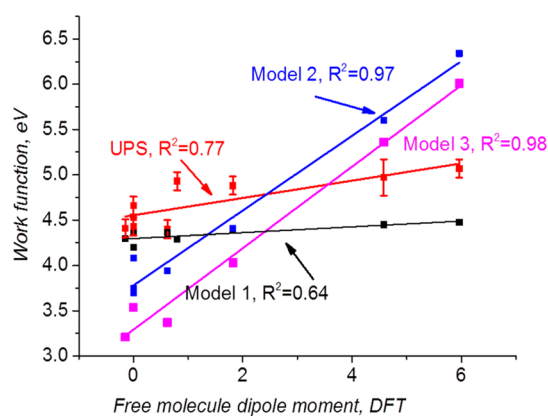
Covalent bonding of aromatic molecules to carbon surfaces by reduction of diazonium reagents has been shown by scanning probe microscopy to nucleate at edge site defects of an otherwise ordered graphite surface, indicating more rapid modification of edge sites followed by slower reactions with basal sites.<sup>49</sup> Surface Raman spectroscopy,<sup>50</sup> as well as theoretical predictions<sup>51</sup> indicate more rapid bonding at edge sites over basal sites in either ordered graphite or graphene sheets. Although the precise geometry of attachment on the disordered PPF surface is difficult to determine, we will assume edge-bonding to graphitic planes during surface modification. Detailed theoretical treatments of graphene sheets and nanoribbons have been reported, which consider the fragment size necessary to approximate bulk properties.<sup>52–55</sup> For the current investigation, the HOMO and LUMO energies of graphene fragments of increasing size were determined, with the results shown in Supporting Information Figure S2 for an H-terminated zigzag fragment. The HOMO–LUMO gap decreases from > 4 eV for benzene to a minimum of 0.06 eV for a 54-ring graphene sheet (designated G54), while ordered graphite has a small overlap of the valence and conduction bands. Therefore, the G54 fragment was selected for investigation of its interactions with chemisorbed molecules in Model 1. Supporting Information Figures S2 and S3 show the effect of graphene sheet size on HOMO and LUMO energies, and the spatial distributions of the HOMO, H-1, LUMO, and L+1 orbitals of G54 for the unmodified G54 fragment.

Figure 2 shows five molecular orbitals and their energies for a Model 1 system containing an azobenzene (AB) molecule bonded to G54 at a zigzag site, with the dihedral angle ( $\theta$ ) between the phenyl rings of the azobenzene and the graphene plane at the optimized value of 65°. The orbitals localized on the G54 moiety are not significantly altered in appearance

compared to unmodified graphene (Supporting Information, Figure S3), implying a minor perturbation of the G54 system due to the attachment of the AB molecule. Also shown in Figure 2 is the H-6 orbital, which is the highest energy orbital with significant localization on the AB moiety. The occupied molecular orbitals HOMO to H-5 are localized on the graphene moiety only, as shown in Supporting Information, Figure S4. In all subsequent discussion, we refer to the highest energy occupied orbital with significant electron density on the molecule bonded to G54 as the “H-X” orbital, and the value of X can vary with molecular structure and torsional angle. Figure 3 shows the effect of dihedral angle ( $\theta$ ) on the HOMO and the highest energy orbital (H-X) with significant localization on the AB moiety for the G54–AB model structure.

Note that the occupied molecular orbital with significant electron density on the AB moiety that is H-6 in the optimized structure shifts down to become H-10 for dihedral angle of 90° and up to become H-5 and H-3 for dihedral angles 45° and 0°. This orbital localized on the AB moiety shifts to a higher energy with decreasing  $\theta$  and becomes delocalized over both the AB and G54 fragments. In real junctions, the AB molecules bonded to PPF are likely to have a range of dihedral angle values, and the angles will be constrained by nearby AB moieties. Figure 3 indicates the important effect of the dihedral angle on the molecular orbital energies and spatial distributions. Figures S4–S6 in the Supporting Information show the spatial distributions and energies of the highest energy orbitals for G54–AB having dihedral angles of  $\theta = 65^\circ$ ,  $33^\circ$ , and  $0^\circ$ , all calculated using Model 1. Figure S7 in Supporting Information presents the effect of dihedral angle on the orbital energies for G54-molecule structures of all eight molecules considered.

An important experimental observable related to the effect of chemical modification of a  $sp^2$  graphitic surface is provided by the work function (see Figure 4), determined with UPS of a



**Figure 4.** Work functions determined from UPS of modified PPF surfaces as a function of the free molecule dipole moments calculated from DFT [BLYP-6-31G(d)] (red points and line). Also shown are work functions calculated using Model 1 and those calculated for graphene surfaces with covalently bonded molecules as in Models 2 and 3. The  $R^2$  values are correlation coefficients for linear fits to the points.

modified electrode surface.<sup>4</sup> For both metallic and PPF surfaces, a molecular mono- or multilayer changes the observed binding energy of a photoelectron by up to 1 eV, as confirmed by Kelvin probe measurements.<sup>56</sup> The effect occurs when the bonded molecule has a dipole moment and has been described as a local vacuum level shift that affects the energy of an electron as it leaves the electrode surface.<sup>44,57,58</sup> For example, a dipole oriented away from the surface withdraws electrons from the electrode, which in turn shifts the local electrostatic potential in the molecular layer. This effect is well known for interfaces between metals and organic films<sup>41–43</sup> and underlies at least part of the compression effect described earlier for molecular tunnel junctions.<sup>30</sup> The work function is the minimum energy required to remove an electron from a solid to a point immediately outside the solid surface, which is the energy needed to move an electron from the Fermi energy level into vacuum. The work function for a single G54 sheet modified with molecules (Model 1) is calculated as the difference in energy between the neutral G54-molecule structure and its cation, and is equivalent to its ionization energy. Because nonperiodic models lack a surface or Fermi energy, the ionization energy is the best analog to a work function for Model 1. For Model 2 and Model 3, the work function is calculated using DMol<sup>3</sup> as the difference between the Fermi energy and the electrostatic potential in vacuum away from the surface. Effectively, DMol<sup>3</sup> computes the Fermi energy for an infinite array of 2D periodic slabs of graphene ribbons separated by wide vacuum spacings and the spatial distribution of the electrostatic potential. This approach yields the electrostatic potential in vacuum and allows determination of the work function. Figure 4 shows a plot of the work functions determined using UPS of six systems containing molecules bonded to PPF vs the free molecule dipole moment calculated using DFT. A shift of 0.7 eV was observed for the PPF/molecule work function, which correlates with the dipole moment and yields a linear correlation coefficient ( $R^2$ ) of 0.77. Table 1 lists the work functions calculated with the three different models.

The work functions (i.e., ionization energies) from Model 1 show a weak correlation with dipole moment, indicating that Model 1 as applied to G54–AB is insufficient for predicting

**Table 1.** Theoretical Work Functions for Three Models

	Model 1 (eV)	Model 2 (eV)	Model 3 (eV)
bare electrode	4.50	3.51	3.13
C8N	4.29	2.39	2.91
PhNO <sub>2</sub>	4.45	5.60	5.36
AQ	4.17	3.75	3.59
BrP	4.39	4.41	4.03
NAB	4.47	6.34	6.01
EB	4.36	3.94	3.37
AB	4.36	4.08	3.54

work functions of modified PPF surfaces. Model 1 describes the junction as a molecule and does not consider removing the electron along a particular direction, i.e. from the contact *through* the molecular layer and into vacuum, as would be the case for UPS or tunnel junction experiments. The dipole and local electrostatic potential shift in the molecular layer are not taken into account in Model 1 but are clearly important for determining the tunneling barrier. As shown below, Model 1 for a single G54–AB structure can be useful for visualizing orbitals and predicting tunnelling barriers, but not for predicting work functions. The main advantage of Model 1, is that it can be treated using the most advanced computational methods, such as hybrid density functionals that include exact exchange.

Calculations with PBC allow the modeling of a graphene surface with molecules covalently bonded to it, analogous to G54–AB molecules stacked along the axis perpendicular to the G54 plane. The calculation is significantly more complex, and allows us to better approximate the real electrode surface. Model 2 extends Model 1 to where the G54 fragment approaches an infinitely large 2D graphene nanoribbon. Model 3 implements the interaction between graphene planes by representing a 3D electrode surface, and is closest to the real electrode. The limitation of Models 2 and 3, however, is in the computational methods implemented in DMol<sup>3</sup>, in particular, the unavailability of DFT methods that calculate exact exchange, which has been highlighted as being very important for accurate prediction of frontier orbitals and the resultant Fermi energy and HOMO–LUMO energy gap.<sup>59</sup> Figure 5 shows several orbitals calculated using Models 1, 2, and 3 for the graphene–AB system.

The results for single- and double-layer PBC models for the seven molecules studied previously are shown in Table 1 and Figure 4, and comparison to Figure 5 leads to several observations. First, note that the work function values calculated for Models 2 and 3 correlate with the dipole moments, although the calculation predicts a steeper slope than that observed by UPS. Second, the dihedral angle  $\theta$  decreases in the low energy configuration from 65° for Model 1 (G54–AB molecule) and 68° for Model 2 to 33° for Model 3. Third, the highest energy orbital showing significant electron density on the molecule is H-1 for Model 2, rather than H-6 for Model 1. Comparison of the HOMO and H-X orbitals for Models 1–3 of AB, EB, and BTB molecular films by both single molecule and PBC approaches (Figure S8 in Supporting Information) shows that the molecular orbital distributions are similar in all three models. As discussed below, these orbitals are likely the most important for determining tunneling current and associated barriers.

We used the method of Kim et al.<sup>4</sup> in our previous report<sup>30</sup> to determine the onset of photoemission from a molecular layer

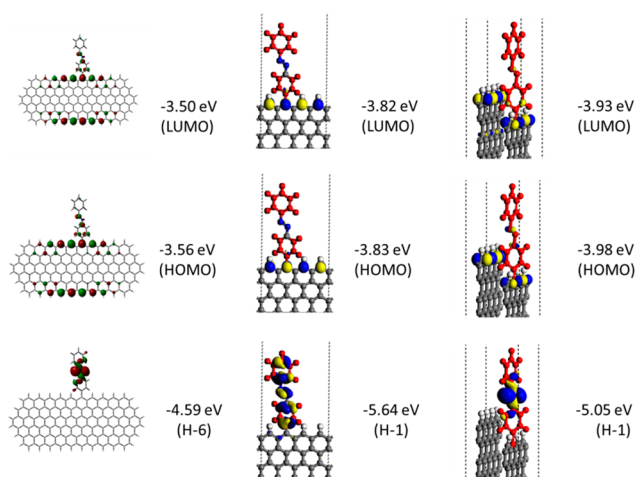


**Figure 5.** HOMO, LUMO, and H-X orbitals for Models 1, 2, and 3 of the graphene-AB system show similarity among the models. The difference between HOMO and H-X energies is the tunnelling barrier listed as  $E_{H,S} - E_{H-X}$  in Table 3.

on PPF from the UPS spectrum at low energies close to the work function. The  $E_f - E_{HOMO, onset}$  thus determined provides an experimental indication of the hole tunnelling barrier and correlates with transport and photocurrent measurements as already noted in Figure 1. For a particular orbital to mediate hole tunneling, it should be localized *between* the two contacts and therefore reside at least partially in the molecular layer.<sup>60–62</sup> The electron in a HOMO does not change energy during tunneling, but it has a finite electron density in the electrode and can move under an applied bias. Using the same logic as the UPS measurements, we postulate that the orbital mediating hole tunneling is the highest H-X orbital (with X being an integer indicating the orbital in Models 1–3) because this orbital has electron density that partially or fully bridges the gap between the two contacts. Referring to orbital diagrams such as Figure 3, we note that the system HOMO of the G54-AB structure is analogous to the Fermi level of modified PPF because it is the highest energy electron in the system and therefore appears at the threshold of photoemission. By this convention, we define the hole tunneling barrier as  $E_{H,S} - E_{H-X}$ , where “S” for “system” refers to the G54-molecule structure, and  $E_{H-X}$  is the closest energy below  $E_{H,S}$  which has significant localization in the molecular layer. For the complementary process of electron tunneling, the corresponding barrier would be  $E_{L+X} - E_{H,S}$ , where L+X is the lowest energy unoccupied orbital of the G54-molecule system that is localized in the molecular layer.

The H-X orbitals for the series of seven aromatic and one aliphatic molecules are shown in Figure 6, and the corresponding hole tunneling barriers are listed as  $E_{H,S} - E_{H-X}$  in Table 2. Note that the identity of the H-X orbital varies significantly for different molecules, and may be much lower in energy than the free molecule HOMO.

Furthermore, the identity and energy of the H-X orbital varies with dihedral angle, since smaller angles results in mixing of the graphene and molecular orbitals. For visualization of orbitals in Figures 3 and 5, we have used the same isovalues and observed the trend showing shifts of energy and electron distribution with dihedral angle that is consistent for all three models. Note also that the hole tunneling barriers for Model 1 range from 1.01 to 2.36 eV for the optimized aromatic

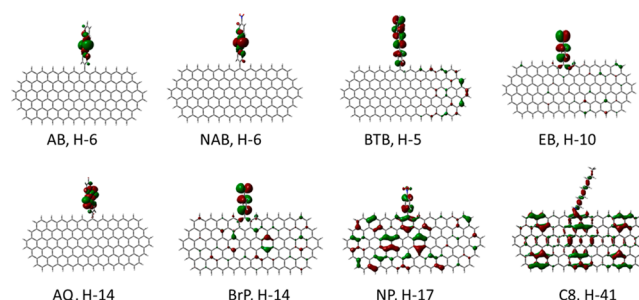


**Figure 6.** Electron density distributions of the highest energy occupied orbitals with significant localization on the attached molecule for seven aromatic and one aliphatic molecule calculated using Model 1 in the optimized geometry. Abbreviations are the same as in Figure 1.

molecules, which is still significantly greater than the  $1.3 \pm 0.2$  eV observed experimentally.<sup>30</sup>

As shown in Table 3, the use of PBC decreases this range to 1.17–2.15 eV for Model 2 and 1.03–2.08 eV for Model 3. As noted earlier, the PBC models also predict a smaller dihedral angle, and some of the compression of the orbital energies is due to stronger electronic coupling between the molecule and graphene for smaller angles. As noted in Table 2, setting smaller angles in Model 1 yields a smaller range of barriers for aromatic molecules of 0.8–1.5 eV for a zero dihedral angle, similar to that predicted for the optimized structures of Models 2 and 3. Figure 5 shows the HOMO, LUMO, and H-X orbitals for the three models, with model 1 set to a 33° dihedral angle. Although the energies and identity of the H-X orbital vary with the model, the HOMO and LUMO lack electron density on the molecule in all cases, and the H-X orbital has significant density localization in the molecular layer. Supporting Information Figures S4 to S6 show the electron distributions for G54-AB for the HOMO to H-7 orbitals at dihedral angles of the optimized angle of 65° as well as 0° and 33°. Figure 5 shows that orbitals for selected molecules and dihedral angles have similar appearance for the three models, and Supporting Information Figure S7 provides the HOMO and H-X energies for all eight molecules considered as a function of dihedral angle.

The computational results for all three models are compared to the experimental results in Figure 7, plotted in the same format as Figure 1, and all using the BLYP functional. The “hole tunneling barrier” on the Y axis is  $E_{H,S} - E_{H-X}$  for the three models considered here, and for the free molecules it is the offset between the calculated HOMO for unmodified G54 (−4.5 eV) and the HOMO of the free molecule alone.

Although all cases shown predict a significantly higher barrier for the alkane compared with the aromatic molecules, the free molecule and Model 1 with optimum  $\theta$  seriously overestimate the tunneling barriers for the aromatic molecules. As noted previously, much of this compression of tunneling barriers results from electronic coupling of the molecule to the electrode, and the effects of molecular dipoles. The compression of tunneling barriers for Models 2 and 3 amounts to a weaker dependence on orbital energy levels than that predicted from the free molecule HOMO levels and is consistent with the weak dependence of observed junction conductance on molecular structure reported for both single-molecule and ensemble devices.<sup>23,30,63,64</sup> An added insight from the current results is that the orbital which mediates tunnelling need not be the molecular HOMO, but rather H-X, the orbital

Table 2. Orbital Energies for G54–Molecule Clusters Calculated with Model 1, All in eV

	optimized <sup>a</sup>			0 degrees <sup>b</sup>			33 degrees <sup>c</sup>		
	$E_{H,S}$	$E_{H-X}$	$E_{H,S} - E_{H-X}$	$E_{H,S}$	$E_{H-X}$	$E_{H,S} - E_{H-X}$	$E_{H,S}$	$E_{H-X}$	$E_{H,S} - E_{H-X}$
G54	-3.49			-3.82					
C8N	-3.38	-7.08	3.7	-3.32	-7.06	3.74			
PhNO <sub>2</sub>	-3.58	-5.94	2.36	-3.70	-5.18	1.48	-3.64	-5.73	2.09
AQ	-3.56	-5.58	2.02	-3.37	-5.12	1.45	-3.61	-5.22	1.61
BrP	-3.345	-5.60	2.15	-3.60	-5.07	1.47	-3.55	-5.07	1.52
NAB	-3.66	-4.93	1.27	-3.72	-4.69	0.97	-3.72	-4.80	1.08
EB	-3.49	-5.37	1.87	-3.58	-4.84	1.26	-3.53	-4.85	1.32
AB	-3.51	-4.72	1.21	-3.62	-4.45	0.83	-3.56	-4.59	1.03
BTB	-3.47	-4.48	1.01	-3.54	-4.39	0.85	-3.49	-4.50	1.01

<sup>a</sup>Dihedral angle in optimized aromatic molecules,  $\sim 65^\circ$ . <sup>b</sup>Dihedral angle set to  $0^\circ$  in an otherwise optimized structure. <sup>c</sup>Dihedral angle set to  $33^\circ$ , which is the optimized angle for Model 3.

Table 3. Orbital Energies and Energy Barriers for Optimized Structures from Models 2 and 3, in eV

	Model 1, $0^\circ$	Model 2			Model 3		
	$E_{H,S} - E_{H-X}$	$E_{H,S}$	$E_{H-X}$	$E_{H,S} - E_{H-X}$	$E_{H,S}$	$E_{H-X}$	$E_{H,S} - E_{H-X}$
G		-3.66			-3.87		
C8N	3.74	-3.67	-7.86	4.19	-3.40	-7.54	4.14
PhNO <sub>2</sub>	1.48	-4.37	-6.52	2.15	-4.43	-6.38	1.95
AQ	1.45	-4.13	-5.82	1.69	-4.02	-5.72	1.70
PhBr	1.47	-3.97	-6.08	2.11	-3.98	-6.05	2.08
NAB	0.97	-4.49	-5.23	1.14	-5.26	-6.19	0.93
PhCCH	1.26	-3.76	-5.70	1.94	-3.77	-5.72	1.95
AB	0.83	-3.75	-4.92	1.17	-4.02	-5.05	1.03
BTB	0.85	-3.69	-4.89	1.20	-3.74	-4.94	1.19

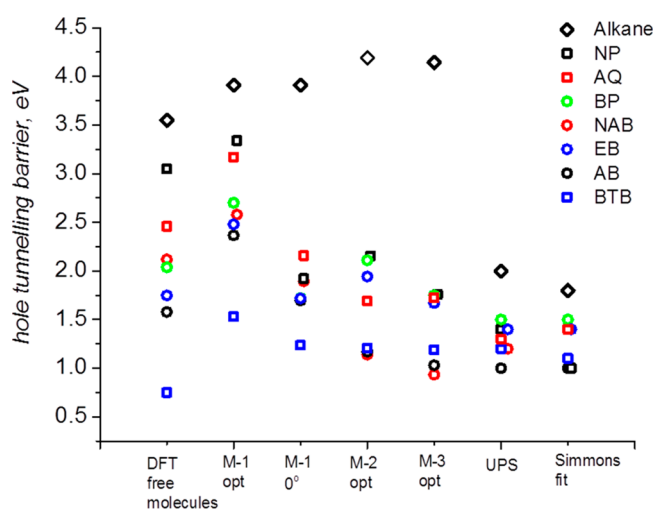


**Figure 7.** Predicted hole tunneling barriers ( $E_{H,S} - E_{H-X}$ ) for various models and dihedral angles, compared to experimentally observed UPS results and to fits of  $JV$  curves to a Simmons model. M-1= Model 1, and so forth; “opt” indicates optimized geometry. Experimental results (UPS and Simmons fit) from ref 30.

with electron density localized between the two contact surfaces. As shown in Figures 3, 5, and 6, the energy of the H-X orbital depends not only on its identity and offset from the system HOMO but also on the dihedral angle between the aromatic molecule and the graphene surface. The most sophisticated and computationally demanding model (Model 3) predicts compression close to that observed experimentally, although the simple Model 1 also shows significant compression when the dihedral angle is forced to  $0^\circ$ . As noted for the experimental tunneling results, the  $\beta$ 's for the

aromatic series of molecules were statistically indistinguishable, so correlations within the range of barriers calculated with Model 3 would be approximate at best. However, we should note that for these two cases a smaller optimized value of  $\theta$  relative to the optimized structure of Model 1 leads to significantly higher electronic coupling between the molecule and graphene and as a result to the compression effect. The origin of the discrepancy between the predicted and experimental barriers for the alkanes evident in Figure 7 is not obvious but may be due to the absence of electronic coupling between the aliphatic molecules and the aromatic substrate. Given this discrepancy, the current approach should be applied to aromatic molecular layers on carbon surfaces, and aliphatic molecules may require alternative theory and validation.

The carbon/molecule/Cu or carbon/molecule/carbon devices studied experimentally consist of covalently bonded oligomers on a flat but disordered  $sp^2$  carbon surface and undoubtedly have a range of dihedral angles between the aromatic plane of the molecule and those in the carbon substrate. Because the theory shows the expected sensitivity of energy levels to the dihedral angle, it is difficult to directly correlate theoretical predictions for particular angles to experimental results. However, it is useful to note that lower dihedral angles result in increased electronic coupling between the molecular layer and the substrate and also lower predicted tunneling barriers. It is quite possible that the molecules with low dihedral angle support significantly higher tunneling currents and that a minority of the available molecules is responsible for a majority of the tunneling current. A corollary to this statement is that control of the dihedral angle should strongly affect tunneling current and may be a fruitful objective of alternative methods to bond aromatic molecules to aromatic

substrates. It also follows that  $sp^2$  carbon differs fundamentally from metal surfaces in this respect and may identify the carbon substrate as unique among electronic conductors.

Finally, the nature of the binding site to disordered  $sp^2$  carbon can vary, at least among the “armchair” and “zigzag” edges in addition to less ordered termination at the edges of the graphene sheets. The question arises of how bonding of an aromatic molecule to such sites affects the H,S and H-X orbital energies, and therefore the predicted tunneling barrier. Figure 8

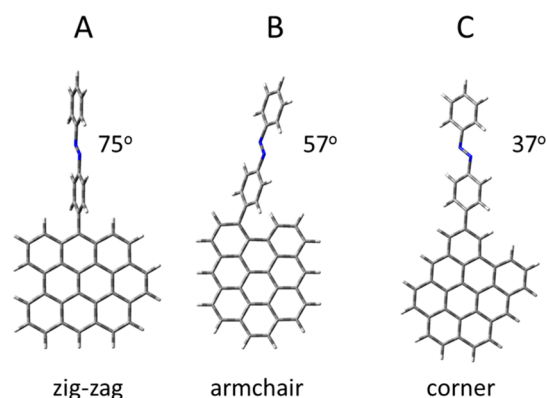


**Figure 8.** Structures used to model azobenzene bonded to different edge sites on a G9 graphene fragment, with their energies for various angles listed in Table 4.

shows three G9 fragments which are H-terminated except for one AB molecule bonded to three possible edge sites. The orbital energies of the three structures were calculated with the BLYP/6-31G(d) parameters, but note that the number of graphene rings is smaller than in the G54 cluster of Model 1.

The optimized dihedral angles differ for the three structures, due to varying steric hindrance between the molecule and the G9 cluster. The  $E_{H,S} - E_{H-X}$  barriers predicted for the optimized structures vary by 0.10 eV, implying a small dependence of the barrier on site geometry. When the dihedral angle is fixed at  $0^\circ$ ,  $33^\circ$ , or  $90^\circ$ , the  $E_{H,S} - E_{H-X}$  barrier for the three configurations varies by 0.02 eV for  $90^\circ$  up to 0.22 eV for  $0^\circ$ . At least for this simple model, the effect of binding site on tunneling barrier is small and should not be a controlling factor in determining electronic behavior. Given the fact that the real molecular junction has a range of dihedral angles and binding sites, orbital energy variations in both parameters are likely averaged into an effective barrier for the entire ensemble of molecules.

## CONCLUSIONS

The correlation between theoretically calculated work functions and tunneling barriers and the experimentally observed results provides important validation of the theory for explaining and predicting real junction behavior. The observed compression of

tunnel barriers in molecular junctions compared to those calculated from free molecule orbital energies was confirmed theoretically and is consistent with the experimental UPS and current density measurements. Although a variety of bonding sites and angles are possible in a system composed of a covalently bonded molecule on a disordered  $sp^2$  hybridized carbon surface, the agreement between theory and experiment for relatively simple model structures indicates that the theory has predictive value for rational design of carbon-based molecular junctions. Model 1, consisting of a G54 cluster with a molecule bonded on a “zig-zag” edge site, allowed us to use advanced computational methods and demonstrated that DFT reveals strong effects of dihedral angle on orbital energies, mixing of orbitals originating on the G54 sheet with those of the attached molecule. Models 2 and 3 with one or two graphene layers in an infinite lattice approach the physical model of the surface and allow calculation of the electronic structure of the system with better accuracy. However, these models are more limited compared to Model 1 in the available DFT methods. When the hole tunneling barrier is defined as the energy difference between the system HOMO and the closest occupied orbital with electron density in the molecular layer, all three models predict the compression observed by UPS and transport measurements. The predictions of Model 1 are significantly closer to the experimental results as the dihedral angle between molecule and graphene approaches zero. Models 2 and 3 using PBC predict a range of tunnel barriers similar to that observed experimentally, but the accuracy of the experimental barriers prevent precise direct comparisons for individual cases. Finally, the dihedral angle between the aromatic plane of the bonded molecule and the graphitic plane of the substrate is an important determinant of orbital energies and electronic coupling, with the type of binding site showing smaller effects. For the general problem of predicting the electronic behavior of carbon-based molecular junctions, the relatively simple Model 1 is useful for visualizing orbitals and the effect of torsion, but Models 2 and 3 are necessary for predicting work functions and more accurate tunneling barriers.

## ASSOCIATED CONTENT

### Supporting Information

Schematics of model calculations and additional orbital diagrams showing electron density distributions as functions of molecular structure and dihedral angles are included. The Supporting Information is available free of charge on the ACS Publications website at DOI: 10.1021/jp5128332.

## AUTHOR INFORMATION

### Corresponding Author

\*E-mail: mcreery@ualberta.ca.

### Notes

The authors declare no competing financial interest.

**Table 4.** Orbital Energies for the Structures of Figure 8, All in eV

	zig-zag			arm-chair			corner		
	$E_{H,S}$	$E_{H-X}$	$E_{H,S}-E_{H-X}$	$E_{H,S}$	$E_{H-X}$	$E_{H,S}-E_{H-X}$	$E_{H,S}$	$E_{H-X}$	$E_{H,S}-E_{H-X}$
optimized	-4.00	-4.72	0.72	-4.02	-4.65	0.63	-4.06	-4.68	0.62
$90^\circ$	-3.99	-4.64	0.65	-3.98	-4.65	0.67	-4.03	-4.61	0.58
$33^\circ$	-4.04	-4.54	0.51	-3.99	-4.53	0.54	-4.06	-4.58	0.52
$0^\circ$	-4.1	-4.42	0.32	-3.95	-4.49	0.54	-4.07	-4.57	0.50

## ■ ACKNOWLEDGMENTS

This work was supported by Natural Sciences and Engineering Research Council of Canada, the National Institute for Nanotechnology, The University of Alberta, and The Province of Alberta. The National Institute for Nanotechnology is operated as a partnership between the National Research Council and the University of Alberta and is jointly funded by the Government of Canada, the Government of Alberta, and the University of Alberta. The authors acknowledge useful conversations with Dr. Adam Bergren.

## ■ REFERENCES

- (1) Simmons, J. G. Generalized Formula for the Electric Tunnel Effect between Similar Electrodes Separated by a Thin Insulating Film. *J. Appl. Phys.* **1963**, *34*, 1793–1803.
- (2) Bergren, A. J.; McCreery, R. L.; Stoyanov, S. R.; Gusarov, S.; Kovalenko, A. Electronic Characteristics and Charge Transport Mechanisms for Large Area Aromatic Molecular Junctions. *J. Phys. Chem. C* **2010**, *114*, 15806–15815.
- (3) Akkerman, H. B.; Naber, R. C. G.; Jongbloed, B.; van Hal, P. A.; Blom, P. W. M.; de Leeuw, D. M.; de Boer, B. Electron Tunneling through Alkanedithiol Self-Assembled Monolayers in Large-Area Molecular Junctions. *Proc. Natl. Acad. Sci. U.S.A.* **2007**, *104*, 11161–11166.
- (4) Kim, B.; Choi, S. H.; Zhu, X. Y.; Frisbie, C. D. Molecular Tunnel Junctions Based on  $\pi$ -Conjugated Oligoacene Thiols and Dithiols between Ag, Au, and Pt Contacts: Effect of Surface Linking Group and Metal Work Function. *J. Am. Chem. Soc.* **2011**, *133*, 19864–19877.
- (5) Luo, L.; Choi, S. H.; Frisbie, C. D. Probing Hopping Conduction in Conjugated Molecular Wires Connected to Metal Electrodes. *Chem. Mater.* **2011**, *23*, 631–645.
- (6) Ellison, D. J.; Kim, J. Y.; Stevens, D. M.; Frisbie, C. D. Determination of Quasi-Fermi Levels across Illuminated Organic Donor/Acceptor Heterojunctions by Kelvin Probe Force Microscopy. *J. Am. Chem. Soc.* **2011**, *133*, 13802–13805.
- (7) Choi, S. H.; Kim, B.; Frisbie, C. D. Electrical Resistance of Long Conjugated Molecular Wires. *Science* **2008**, *320*, 1482–1486.
- (8) Burin, A. L.; Berlin, Y. A.; Ratner, M. A. Semiclassical Theory for Tunneling of Electrons Interacting with Media. *J. Phys. Chem. A* **2001**, *105*, 2652–2659.
- (9) Buttiker, M.; Landauer, R. Traversal Time for Tunneling. *Phys. Rev. Lett.* **1982**, *49*, 1739.
- (10) Lindsay, S. M.; Ratner, M. A. Molecular Transport Junctions: Clearing Mists. *Adv. Mater.* **2007**, *19*, 23–31.
- (11) Li, Z.; Smeu, M.; Afsari, S.; Xing, Y.; Ratner, M. A.; Borguet, E. Single-Molecule Sensing of Environmental pH—an STM Break Junction and NEGF-DFT Approach. *Angew. Chem., Int. Ed.* **2014**, *53*, 1098–1102.
- (12) Reuter, M. G.; Seideman, T.; Ratner, M. A. Molecular Conduction through Adlayers: Cooperative Effects Can Help or Hamper Electron Transport. *Nano Lett.* **2011**, *11*, 4693–4696.
- (13) Huisman, E. H.; Guedon, C. M.; van Wees, B. J.; van der Molen, S. J. Interpretation of Transition Voltage Spectroscopy. *Nano Lett.* **2009**, *9*, 3909–3913.
- (14) Malen, J. A.; Doak, P.; Baheti, K.; Tilley, T. D.; Segalman, R. A.; Majumdar, A. Identifying the Length Dependence of Orbital Alignment and Contact Coupling in Molecular Heterojunctions. *Nano Lett.* **2009**, *9*, 1164–1169.
- (15) Amdursky, N.; Marchak, D.; Sepunaru, L.; Pecht, I.; Sheves, M.; Cahen, D. Electronic Transport Via Proteins. *Adv. Mater.* **2014**, *26*, 7142–7161.
- (16) Salomon, A.; Cahen, D.; Lindsay, S.; Tomfohr, J.; Engelkes, V. B.; Frisbie, C. D. Comparison of Electronic Transport Measurements on Organic Molecules. *Adv. Mater.* **2003**, *15*, 1881–1890.
- (17) Batra, A.; Kladnik, G.; Vázquez, H.; Meisner, J. S.; Floreano, L.; Nuckolls, C.; Cvetko, D.; Morgante, A.; Venkataraman, L. Quantifying

through-Space Charge Transfer Dynamics in  $\pi$ -Coupled Molecular Systems. *Nat. Commun.* **2012**, *3*, 1086.

(18) Cheng, Z. L.; Skouta, R.; Vazquez, H.; Widawsky, J. R.; Schneebeli, S.; Chen, W.; Hybertsen, M. S.; Breslow, R.; Venkataraman, L. In Situ Formation of Highly Conducting Covalent Au-C Contacts for Single-Molecule Junctions. *Nat. Nanotechnol.* **2011**, *6*, 353–357.

(19) Darancet, P.; Widawsky, J. R.; Choi, H. J.; Venkataraman, L.; Neaton, J. B. Quantitative Current–Voltage Characteristics in Molecular Junctions from First Principles. *Nano Lett.* **2012**, *12*, 6250–6254.

(20) Chen, F.; Tao, N. J. Electron Transport in Single Molecules: From Benzene to Graphene. *Acc. Chem. Res.* **2009**, *42*, 429–438.

(21) Makk, P.; Tomaszewski, D.; Martinek, J.; Balogh, Z.; Csonka, S.; Wawrzyniak, M.; Frei, M.; Venkataraman, L.; Halbritter, A. Correlation Analysis of Atomic and Single-Molecule Junction Conductance. *ACS Nano* **2012**, *6*, 3411–3423.

(22) Venkataraman, L.; Klare, J. E.; Nuckolls, C.; Hybertsen, M.; Steigerwald, M. L. Dependence of Single-Molecule Junction Conductance on Molecular Conformation. *Nature* **2006**, *442*, 904–907.

(23) Venkataraman, L.; Park, Y. S.; Whalley, A. C.; Nuckolls, C.; Hybertsen, M. S.; Steigerwald, M. L. Electronics and Chemistry: Varying Single-Molecule Junction Conductance Using Chemical Substituents. *Nano Lett.* **2007**, *7*, 502–506.

(24) Reus, W. F.; Nijhuis, C. A.; Barber, J. R.; Thuo, M. M.; Tricard, S.; Whitesides, G. M. Statistical Tools for Analyzing Measurements of Charge Transport. *J. Phys. Chem. C* **2012**, *116*, 6714–6733.

(25) Reuter, M. G.; Harrison, R. J. Rethinking First-Principles Electron Transport Theories with Projection Operators: The Problems Caused by Partitioning the Basis Set. *J. Chem. Phys.* **2013**, *139*, -.

(26) Bilić, A.; Reimers, J. R.; Hush, N. S. The Structure, Energetics, and Nature of the Chemical Bonding of Phenylthiol Adsorbed on the Au(111) Surface: Implications for Density-Functional Calculations of Molecular-Electronic Conduction. *J. Chem. Phys.* **2005**, *122*, -.

(27) Xue, Y.; Datta, S.; Ratner, M. A. First-Principles Based Matrix Green's Function Approach to Molecular Electronic Devices: General Formalism. *Chem. Phys.* **2002**, *281*, 151–170.

(28) Yan, H.; Bergren, A. J.; McCreery, R.; Della Rocca, M. L.; Martin, P.; Lafarge, P.; Lacroix, J. C. Activationless Charge Transport across 4.5 to 22 nm in Molecular Electronic Junctions. *Proc. Natl. Acad. Sci. U.S.A.* **2013**, *110*, 5326–5330.

(29) McCreery, R.; Yan, H.; Bergren, A. J. A Critical Perspective on Molecular Electronic Junctions: There Is Plenty of Room in the Middle. *Phys. Chem. Chem. Phys.* **2013**, *15*, 1065–1081.

(30) Sayed, S. Y.; Fereiro, J. A.; Yan, H.; McCreery, R. L.; Bergren, A. J. Charge Transport in Molecular Electronic Junctions: Compression of the Molecular Tunnel Barrier in the Strong Coupling Regime. *Proc. Natl. Acad. Sci. U.S.A.* **2012**, *109*, 11498–11503.

(31) Bergren, A. J.; McCreery, R. L. Analytical Chemistry in Molecular Electronics. *Annu. Rev. Anal. Chem.* **2011**, *4*, 173–195.

(32) McCreery, R. L.; Bergren, A. J. Progress with Molecular Electronic Junctions: Meeting Experimental Challenges in Design and Fabrication. *Adv. Mater.* **2009**, *21*, 4303–4322.

(33) Anariba, F.; DuVall, S. H.; McCreery, R. L. Mono- and Multilayer Formation by Diazonium Reduction on Carbon Surfaces Monitored with Atomic Force Microscopy “Scratching”. *Anal. Chem.* **2003**, *75*, 3837–3844.

(34) Ranganathan, S.; McCreery, R. L. Electroanalytical Performance of Carbon Films with Near-Atomic Flatness. *Anal. Chem.* **2001**, *73*, 893–900.

(35) Mahmoud, A. M.; Bergren, A. J.; Pekas, N.; McCreery, R. L. Towards Integrated Molecular Electronic Devices: Characterization of Molecular Layer Integrity During Fabrication Processes. *Adv. Funct. Mater.* **2011**, *21*, 2273–2281.

(36) Ru, J.; Szeto, B.; Bonifas, A.; McCreery, R. L. Microfabrication and Integration of Diazonium-Based Aromatic Molecular Junctions. *ACS Appl. Mater. Interfaces* **2010**, *2*, 3693–3701.

- (37) Sayed, S. Y.; Bayat, A.; Kondratenko, M.; Leroux, Y.; Hapiot, P.; McCreery, R. L. Bilayer Molecular Electronics: All-Carbon Electronic Junctions Containing Molecular Bilayers Made with “Click” Chemistry. *J. Am. Chem. Soc.* **2013**, *135*, 12972–12975.
- (38) Yan, H.; Bergren, A. J.; McCreery, R. L. All-Carbon Molecular Tunnel Junctions. *J. Am. Chem. Soc.* **2011**, *133*, 19168–19177.
- (39) Fereiro, J. A.; McCreery, R. L.; Bergren, A. J. Direct Optical Determination of Interfacial Transport Barriers in Molecular Tunnel Junctions. *J. Am. Chem. Soc.* **2013**, *135*, 9584–9587.
- (40) Braun, S.; Salaneck, W. R.; Fahlman, M. Energy-Level Alignment at Organic/Metal and Organic/Organic Interfaces. *Adv. Mater.* **2009**, *21*, 1450–1472.
- (41) Ishii, H.; Sugiyama, K.; Ito, E.; Seki, K. Energy Level Alignment and Interfacial Electronic Structures at Organic/Metal and Organic/Organic Interfaces. *Adv. Mater.* **1999**, *11*, 605–625.
- (42) Hwang, J.; Wan, A.; Kahn, A. Energetics of Metal–Organic Interfaces: New Experiments and Assessment of the Field. *Mater. Sci. Eng., R* **2009**, *64*, 1–31.
- (43) Cahen, D.; Kahn, A. Electron Energetics at Surfaces and Interfaces: Concepts and Experiments. *Adv. Mater.* **2003**, *15*, 271–277.
- (44) Salomon, A.; Boecking, T.; Seitz, O.; Markus, T.; Amy, F.; Chan, C.; Zhao, W.; Cahen, D.; Kahn, A. What Is the Barrier for Tunneling through Alkyl Monolayers? Results from N- and P-Si–Alkyl/Hg Junctions. *Adv. Mater.* **2007**, *19*, 445–450.
- (45) Frisch, M. J.; Trucks, G. W.; Schlegel, H. B.; Scuseria, G. E.; Robb, M. A.; Cheeseman, J. R.; Scalmani, G.; Barone, V.; Mennucci, B.; Petersson, G. A. et al. Gaussian 09; Gaussian, Inc.: Wallingford, CT, 2009.
- (46) Becke, A. D. Density-Functional Exchange-Energy Approximation with Correct Asymptotic-Behavior. *Phys. Rev. A* **1988**, *38*, 3098–3100.
- (47) Perdew, J. P.; Chevary, J. A.; Vosko, S. H.; Jackson, K. A.; Pederson, M. R.; Singh, D. J.; Fiolhais, C. Atoms, Molecules, Solids, and Surfaces - Applications of the Generalized Gradient Approximation for Exchange and Correlation. *Phys. Rev. B* **1992**, *46*, 6671–6687.
- (48) DMOL<sup>3</sup>, Release 4.0; Accelrys, Inc., San Diego, CA, 2001.
- (49) Kariuki, J. K.; McDermott, M. T. Nucleation and Growth of Functionalized Aryl Films on Graphite Electrodes. *Langmuir* **1999**, *15*, 6534–6540.
- (50) Ray, K. G.; McCreery, R. L. Spatially Resolved Raman Spectroscopy of Carbon Electrode Surfaces: Observations of Structural and Chemical Heterogeneity. *Anal. Chem.* **1997**, *69*, 4680–4687.
- (51) Jiang, D. e.; Sumpter, B. G.; Dai, S. How Do Aryl Groups Attach to a Graphene Sheet? *J. Phys. Chem. B* **2006**, *110*, 23628–23632.
- (52) Hod, O.; Peralta, J. E.; Scuseria, G. E. Edge Effects in Finite Elongated Graphene Nanoribbons. *Phys. Rev. B* **2007**, *76*, 233401.
- (53) Barone, V.; Hod, O.; Scuseria, G. E. Electronic Structure and Stability of Semiconducting Graphene Nanoribbons. *Nano Lett.* **2006**, *6*, 2748–2754.
- (54) Ezawa, M. Peculiar Width Dependence of the Electronic Properties of Carbon Nanoribbons. *Phys. Rev. B* **2006**, *73*, 045432.
- (55) Han, M. Y.; Ozyilmaz, B.; Zhang, Y. B.; Kim, P. Energy Band-Gap Engineering of Graphene Nanoribbons. *Phys. Rev. Lett.* **2007**, *98*, 206805.
- (56) Yan, H.; McCreery, R. L. Anomalous Tunneling in Carbon/Alkane/TiO<sub>2</sub>/Gold Molecular Electronic Junctions: Energy Level Alignment at the Metal/Semiconductor Interface. *ACS Appl. Mater. Interfaces* **2009**, *1*, 443–451.
- (57) Qi, Y.; Yaffe, O.; Tirosh, E.; Vilan, A.; Cahen, D.; Kahn, A. Filled and Empty States of Alkanethiol Monolayer on Au (111): Fermi Level Asymmetry and Implications for Electron Transport. *Chem. Phys. Lett.* **2011**, *511*, 344–347.
- (58) Nesher, G.; Vilan, A.; Cohen, H.; Cahen, D.; Amy, F.; Chan, C.; Hwang, J.; Kahn, A. Energy Level and Band Alignment for GaAs–Alkylthiol Monolayer–Hg Junctions from Electrical Transport and Photoemission Experiments. *J. Phys. Chem. B* **2006**, *110*, 14363–14371.
- (59) Xiao, H.; Tahir-Kheli, J.; Goddard, W. A. Accurate Band Gaps for Semiconductors from Density Functional Theory. *J. Phys. Chem. Lett.* **2011**, *2*, 212–217.
- (60) Li, Z.; Borguet, E. Determining Charge Transport Pathways through Single Porphyrin Molecules Using Scanning Tunneling Microscopy Break Junctions. *J. Am. Chem. Soc.* **2011**, *134*, 63–66.
- (61) Li, Z.; Smeu, M.; Ratner, M. A.; Borguet, E. Effect of Anchoring Groups on Single Molecule Charge Transport through Porphyrins. *J. Phys. Chem. C* **2013**, *117*, 14890–14898.
- (62) Xing, Y.; Park, T.-H.; Venkatramani, R.; Keinan, S.; Beratan, D. N.; Therien, M. J.; Borguet, E. Optimizing Single-Molecule Conductivity of Conjugated Organic Oligomers with Carbodithioate Linkers. *J. Am. Chem. Soc.* **2010**, *132*, 7946–7956.
- (63) Yoon, H. J.; Bowers, C. M.; Baghbanzadeh, M.; Whitesides, G. M. The Rate of Charge Tunneling Is Insensitive to Polar Terminal Groups in Self-Assembled Monolayers in Ag<sup>TS</sup>S(CH<sub>2</sub>)<sub>n</sub>M(CH<sub>2</sub>)<sub>m</sub>T//Ga<sub>2</sub>O<sub>3</sub>/EGaIn Junctions. *J. Am. Chem. Soc.* **2013**, *136*, 16–19.
- (64) Yoon, H. J.; Shapiro, N. D.; Park, K. M.; Thuo, M. M.; Soh, S.; Whitesides, G. M. The Rate of Charge Tunneling through Self-Assembled Monolayers Is Insensitive to Many Functional Group Substitutions. *Angew. Chem., Int. Ed.* **2012**, *51*, 4658–4661.